ISSN: 2993-5326

Research Article

Journal of Applied Surface Science

Interaction of Nitrogen-Containing Reagents with the Surface of Syngle-Crystalline Germanium and Optical Properties of Films Obtained by Evaporation of Resulting Germanium Nitride

Irakli Nakhutsrishvili[1*], Zurab Adamia[2] and Nino Sepashvili[1]

[1]*Georgian Technical University, Tbilisi*

[2]*Sukhumi State University, Georgia*

***Corresponding Author**
Irakli Nakhutsrishvili, Georgian Technical University, Tbilisi, Georgia.

Submitted: 2024, Nov 13; **Accepted:** 2024, Dec 02; **Published:** 2024, Dec 17

Citation: Nakhutsrishvili, I., Adamia, Z., Sepashvili, N. (2024). Interaction of Nitrogen-Containing Reagents with the Surface of Syngle-Crystalline Germanium and Optical Properties of Films Obtained by Evaporation of Resulting Germanium Nitride. *J Applied Surf Sci, 2*(2), 01-09.

Abstract

The influence of the secondary process of evaporation of the reaction product on the kinetics of interaction of gases (O_2, Cl_2, NH_3, H_2O and N_2H_4 vapors) with the surface of some metals (Cr, Pb, Si, Ge) and compounds (BN, SiO_2, SiC) is discussed. Also is considered the case when the growth of the scale is preceded by the process of gas etching of the metal surface. A general equation is given that describes the scale growth-evaporation kinetic (sample mass change - time) curves during the interaction of gases with the surface of metals and compounds. Special cases of parabolic, cubic and fourth degree processes are discussed. The kinetics of nitridation of the surface of single-crystaline germanium by ammonia and hydrazine vapors was studied in detail. By evaporating the nitride formed on the germanium surface, a film of germanium oxyntride is deposited on a substrate located in the cold zone of the reactor. The optical characteristics of these films are studied.

Keywords: Scale Growth-Evaporation, Germanium Nitride, Germanium Oxynitride Films

1. Introduction

This work is a continuation of where the role of reduction of the reaction surface and evaporation of scale in the process of oxidation of chromium-containing alloys is considered [1]. Here we will consider in more detail the influence of the secondary process of evaporation (sublimation) on the formal kinetics (mass change - time) of the interaction of gases (O_2, Cl_2, NH_3, H_2O and N_2H_4 vapors) with some metals and compounds. We used data from various works collected, the results of the indicated author, as well as your data [2].

The process of scale formation with its simultaneous evaporation significantly changes the kinetics of the process. When the overall kinetics is determined not by the rate of the chemical reaction itself, but by the diffusion of ions in the scale (volume diffusion), then the kinetics is parabolic and is called the Tedmon's process (although a similar case was discussed somewhat earlier [3-12]. In the case of short-circuit diffusion, cubic kinetics takes place, and in the case of local electric fields and volume charges, the kinetic law of the fourth degree is realized [13-17].

All of the above is clearly shown in the kinetic dependences of the mass gain, which are presented in the figure 1. Here M is total mass change per unit area at the time t and m is a specific mass gain of oxidized object due to reacted oxigen.

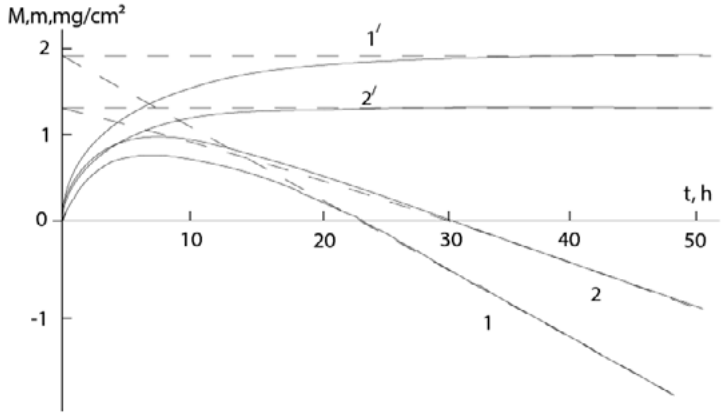

Figure 1: Kinetic Curves: (1) for reaction $Cr+2HCl=CrCl_2+H_2$ at 750°C and (2) $4Cr+3O_2=2CrO_3$ at 1200°C; 1',2' – dependences m – t [18,19]

The slopes of the straight lines in Fig.1 corresponds to the rate of the mass decrease of the sample (v_m) due to the metallic component of the reaction product (Here we consider the coordinate systems t - m and t - M; another coordinate system t_W – W is considered in section 1.2.) To determine of reaction order (n), we can use the formula [20]:

$$n=\frac{\lg[(1-qk)(\bar{M}+v_m\bar{t})/pm_{max}]}{\lg[(\bar{M}+v_m\bar{t})/m_{max}]}, \qquad (1)$$

where $q = v_m / v_g$, $p = (v_m+v_g) / v_g = q+1$ (v_m is the speed of the system mass reduction due to the metal component of the evaporating part of the scale, v_g is the evaporation rate of reaction products by the gaseous component), k_r is rectilinear constant (dm/dt at the origin of coordinate system) and $k = v_g / (k_r-v_g)$. The tangents of the curves in Fig. 1 virtually coincide with ordinate axis at the origin of the coordinates: $k_r \to \infty \Rightarrow k \to 0$. In this case formula (1) is simplified as follows:

$$n=\frac{\lg[(\bar{M}+v_m t)/pm_{max}]}{\lg[(\bar{M}+v_m t)/m_{max}]}. \qquad (2)$$

According to formula (2) for it turns out n≅2.02, and for n≅3.75, that are approaching to 2 and [18,19]. Corresponding empirical expressions are: $t \cong -15.707\ln(1-0.554m)-8.693m$ and $t\cong 28.885\{[0.577\,\mathrm{arctg}((1.424m)/(0.822m+2)]-[0.167\ln((1-0.822m)^2/(m^2+0.822m+1))]\} - 23.75m$, where m is in mg/cm^2 and t is in hours. The curves constructed using these equations on the scale used in Fig.1 practically coincide with the experimental curves.

The rate of mass increase due to the reacted gas in the general case is:

$$\frac{dm}{dt} = \frac{k_n/n}{m^{n-1}+(k_n/nr_r)} - v_g, \qquad (3)$$

where n=2, 3 or 4; $k_r \equiv dm/dt$ (at point t=0,m=0) is rectilinear constant; k_n is the power-law constant. Its integral form is as follows:

$$t=(1+k)\frac{m_{max}^{n-1}}{v_g}\int \frac{dm}{m_{max}^{n-1}-m^{n-1}} - \frac{m}{v_g}, \qquad (4)$$

where $k = v_g / (k_r - v_g)$, and $m_{max} = (k_n / nk_r k)^{1/(n-1)}$ is the maximum mass gain of the system at the expense of active gas. Boundary condition for solving of Eq. (2) for different n is t=0, m=0.

The Tedmon-Wajsel equation (n=2) in our notation will be:

$$t=-(1+k)\frac{m_{max}}{v_g}\ln\frac{m_{max}-m}{m_{max}} - \frac{m}{v_g}. \qquad (5)$$

For n=3 and 4 we will have:

$$t=(1+k)\frac{m_{max}}{2v_g}\ln\frac{m_{max}+m}{m_{max}-m} - \frac{m}{v_g}, \qquad (6)$$

$$t=(1+k)\frac{m_{max}}{v_g}\left[\frac{1}{\sqrt{3}}\mathrm{arctg}\frac{\sqrt{3}m}{m+2m_{max}} - \frac{1}{6}\ln\frac{(m_{max}-m)^2}{m^2+mm_{max}+m_{max}^2}\right] - \frac{m}{v_g}, \qquad (7)$$

respectively [20]. For the total mass change will be:

$$M=m-v_m t. \quad (8)$$

Such containing maxima curves were obtained in a number of works, in works collected, and others [2,18-28]. Here we will look at graphs in which this maximum is clearly expressed and from which reliable information can be obtained (some graphs, which are not considered here, give unrealistic values of kinetic parameters).

2. Experimental

In the experiments, we used plates of single-crystalline germanium of N-type conductivity and with concentration of charge carriers $n=2\cdot10^{20}$ m^{-3}. They were successively degreased in boiling toluene, dried in the air, etched in a liquid etchant CP-4A ($HF:HNO_3$: CH_3COOH = 1:15:1) for (4-5) min and, washed in running distilled water, followed by drying. Ammonia (freezing point -33.4°C) was dried by slowly passing it through a trap cooled with a mixture of liquid nitrogen and alcohol or ice with NaCl. The pressure of ammonia was $P_{NH3}=2.7\cdot10^3$Pa, and pressure of hydrazine $P_{N2H4}=2\cdot10^3$Pa (saturated vapor pressure of N_2H_4 at room temperature). In the case of ammonia, water vapor was deliberately introduced into the reactor: $P\equiv P_{H2O}/P_{NH3}\cong2$ and 5%. The nitridation temperature was (680-820) oC. The temperature of the electric heater was regulated using a high-precision regulator ვრტ (VRT)-3 with an accuracy of ±0.5 °C. Kinetic measurements were carried out by continuously weighing the samples during the oxidation process. For this purpose, a homemade microbalance built into a vacuum unit was used (sensitivity≅10^{-6}g). Electromagnetic compensation for changes in the sample mass was carried out automatically.

3. Results and Discussion

3.1. Analysis of kinetic curves of mass change during the interaction of active gases with the surface of certain metals and compounds with simultaneous evaporation of the products of reaction.

3.1.1. Kinetic Curves of the Total Mass Change, Having a Maximum

As mentioned above, kinetic curves containing a maximum are presented in many works. Most of them are curves corresponding to parabolic kinetics (n=2); there is little data for n=4; but for n=3 we did not find such data, although cubic processes (with curves without maxima) are considered in a fairly large number of works.

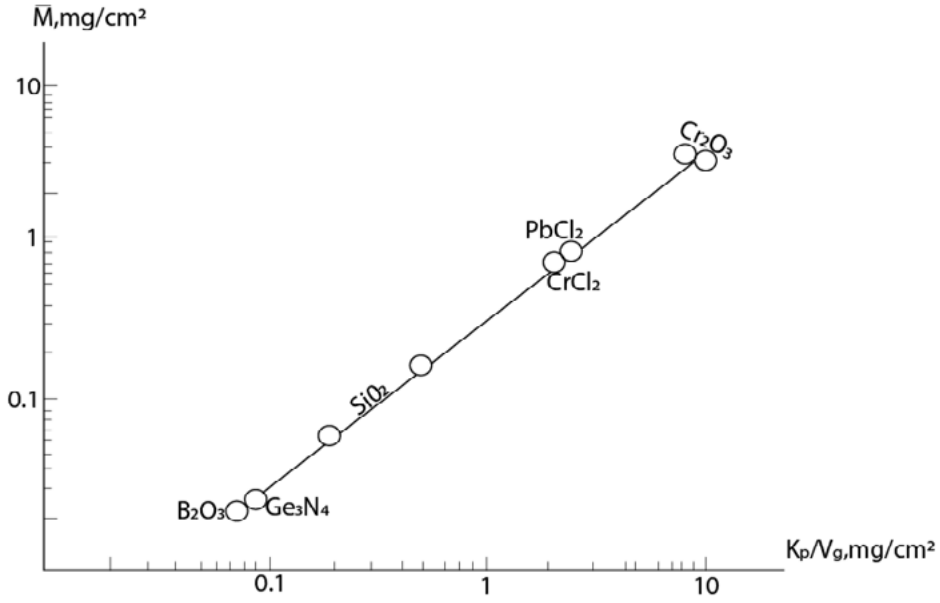

Figure 2: Dependence $\bar{M} - k_p / v_g$ for Different Samples in Logarithmic Coordinates

Figure 2 shows the dependence in coordinates $lg(k_p/v_g)$ - $lg\bar{M}$ for different samples from [2]. The following reactions are considered here: $2Cr+3O_2=Cr_2O_3$, $Pb+Cl_2=PbCl_2$, $Si+O_2=SiO_2$, $SiC+2O_2=SiO_2+CO_2$, $Si_3N_4+3O_2=3SiO_2+2N_2$ and $4BN+3O_2 = 2B_2O_3 +2N_2$ (for all reactions the kinetics are parabolic: k_p - power-law constant at n=2). We have added data for reactions $Cr+2HCl=CrCl_2+H_2$ and $3Ge+4NH_3=Ge_3N_4+6H_2$ (also with parabolic kinetics). This data fit well into this dependence.

3.1.2. Consideration of Preliminary Mass Reduction

In some cases, the growth of scale is preceded by other processes, for example, gas etching of the surface of the metal or alloy (initial section of curve 1 in coordinate system t-W). In this case, to describe the m – t dependence, it is necessary to solve the differential equation (1) with the boundary condition t = 0, m = m_0. For n=2, 3 and 4 these solutions have the form:

$$t=-(1+k)\frac{m_{max}}{v_g}\ln\frac{m_{max}-m}{m_{max-m_0}}-\frac{m-m_0}{v_g}, \quad (9)$$

$$t=(1+k)\frac{m_{max}}{2v_g}\ln\frac{(m_{max}+m)(m_{max}-m_0)}{(m_{max}-m)(m_{max}+m_0)}-\frac{m-m_0}{v_g}, \quad (10)$$

$$t=(1+k)\frac{m_{max}}{v_g}\left[\frac{1}{\sqrt{3}}\text{arctg}\frac{\sqrt{3}m(m-m_0)}{m+2m_{max}}-\frac{1}{6}\ln\frac{(m_{max}-m)^2(m_0^2+m_0m_{max}+m_{max}^2)}{(m_{max}-m_0)^2(m^2+mm_{max}+m_{max}^2)}\right]-\frac{m-m_0}{v_g}, \quad (11)$$

respectively. To demonstrate, we present data on the interaction of single-crystalline Ge with NH_3+H_2O and N_2H_4 vapors.

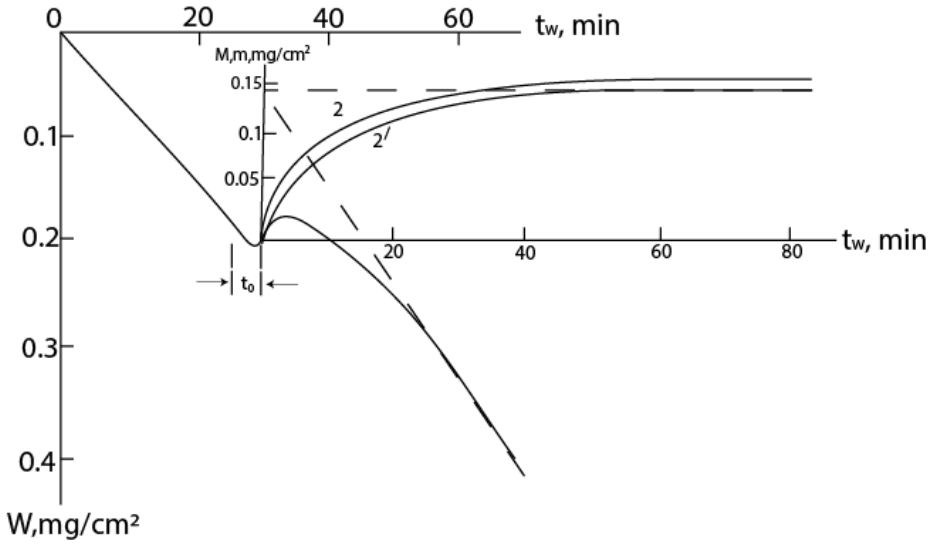

(a)

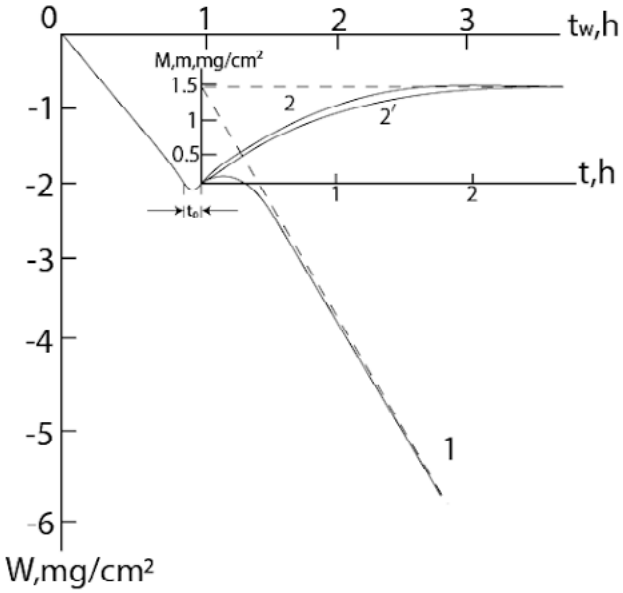

(b)

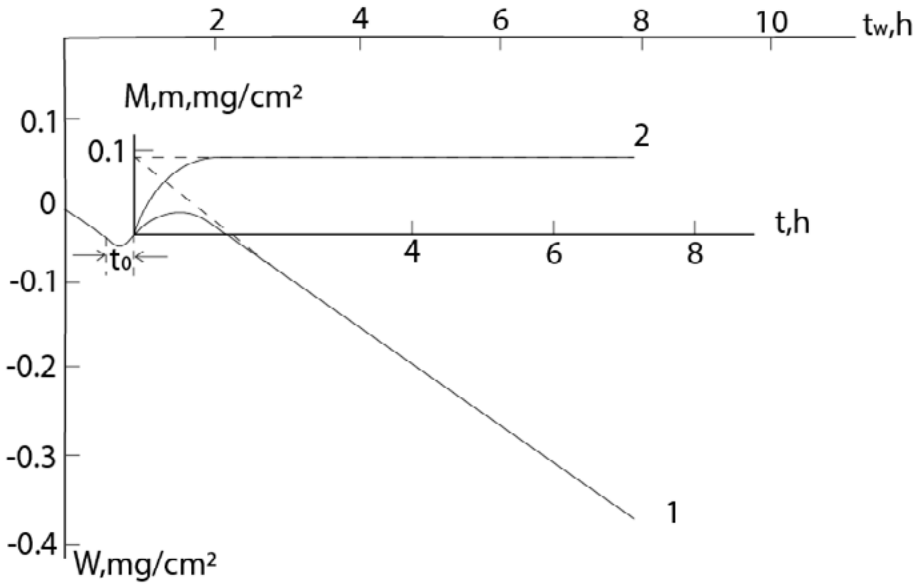

(c)

Figure 3: Kinetic Dependences of Interaction of Ge: with NH_3+H_2O at (a) P=2%, 820°C, (b) P=5%, 800°C, ($P\equiv_{PH2O}/P_{NH3}$); and (c) with N_2H_4 ($P_{N2H4}=2\cdot10_3$Pa) at 720°C – (1) dependences W – t, (2) – dependences m – t; 2' – calculated curves (in the scale of the figure (c), the experimental and calculated curves practically coincide with each other)

On these curves, the initial decrease of mass is due to the etching of the germanium surface by water vapor, which is contained in small quantities also in concentrated hydrazine (volatile GeO is formed here [29,30]: $GeO+H_2O=GeO+H_2$). Also, it is obvious that the formation of nitride on the germanium surface will begin before the zero point in the t - m coordinate system. But from the presented model it follows that the m - t dependences are convex in the positive direction. Time shifts between equations (3) and (9), (4) and (10), (5) and 11) are:

$$t_0=(1+k)\frac{m_{max}}{v_g}\ln\frac{m_{max}-m_0}{m_{max}}+\frac{m_0}{v_g}, \qquad (9')$$

$$t_0=(1+k)\frac{m_{max}}{2v_g}\ln\frac{m_{max}+m_0}{m_{max}-m_0}+\frac{m_0}{v_g}, \qquad (10')$$

and

$$t_0=(1+k)\frac{m_{max}}{v_g}\left[\frac{1}{6}\ln\frac{(m_{max}-m_0)^2}{m_0{}^2+m_0m_{max}+m_{max}^2}-\frac{1}{\sqrt{3}}\mathrm{arctg}\frac{\sqrt{3}m_0}{m_0+2m_{max}}\right]+\frac{m_0}{v_g}, \qquad (11')$$

respectively. Thus, the values of m0 can be estimated by solving of transcendental equations (9')-(11') by substituting the values of k, m_{max}, v_g, and t_0 determined from experimental data. The main difficulty is the accurate determination of t0 in the initial section of the curves - conducting an additional experiment of short duration would lead to even larger errors.

According to the experimental data presented in Fig.3, one can estimate $t_0\approx$-3 min, -0.14 h, and -0.33 h, respectively with Figs(a), (b) and (c). Then the values of m0 will be ≈0.3, 0.05 and 0.03 mg/cm2. As you can see, m0 makes up (20-34)% of corresponding m_{max} (0.145, 1.42, 0.092 mg/cm^2, respectively) and this cannot be ignored when conducting an experiment using the gravimetric method.

Footnote:

When active gases interact with metal or alloy surface, processes often occur in which compounds of doping impurities are formed. These compounds can create diffusion barriers that prevent the main reaction from occurring. This is equivalent to a decrease in the area of the reaction surface. The corresponding kinetic equations have been derived for such processes. The situation is complicated by the simultaneous occurrence of the processes of evaporation of the main compound and a decrease in the reaction surface. In paper 1, it is indicated that the solution of the corresponding differential equation cannot be expressed using elementary functions. It would be possible to compile tables similar to some known functions, but this would be of interest only for the problem under consideration. Moreover,

at present it is possible to construct the necessary graphs using computer programs without considering mathematical formulas.

3.2. Optical Properties of Germanium Oxynitride Films

As indicated above, when ammonia or hydrazine vapor interacts with the germanium surface, its nitride and monoxide are formed and evaporate. They are deposited in the "cold" (300-350)°C zone of the reactor, where the sapphire substrates were located. An amorphous film of germanium oxynitride was deposited on them.

In this section, we investigate the optical properties of germanium oxynitride films, which are of interest to many areas of science and technology [31-42]. Below we present data for germanium oxynitride film obtained by nitridation of germanium with ammonia.

The studied samples were obtained according to the method described in [43]. Infrared (IR) absorption spectra of the samples were recorded using a spectrometer Nicolet-740-FTIR. Electronic absorption spectra were recorded on a spectrophotometer SF-26-A.

The study of the IR spectra of the films (Figure 4) showed the appearance of one intense band. Its position changes in the region of (780-820) cm^{-1} depending on the temperature of their preparation. As is known, the IR absorption band of the valence vibration of the Ge - N bond, located about 750 cm^{-1}, shifts to the short-wave region of the spectrum as a result of the substitution of nitrogen atoms by oxygen atoms in the $Ge(N_4)$ tetrahedra. Therefore, the bands in Fig.4 can be attributed to $Ge(N_{4-x}O_x)$ type tetrahedra with a random distribution of oxygen atoms in the structural network of the nitride. The only band located between the Ge_3N_4 (~750 cm^{-1}) and GeO_2 (~890 cm^{-1}) bands excludes the existence of separate nitride and oxide phases. It indicates the presence of germanium oxynitride. The shift of the IR band towards lower frequencies is associated with a decrease in the oxygen content in the film with an increase in the temperature of their preparation.

The deposition of oxynitride was also mentioned earlier during vacuum evaporation of Ge_3N_4 in the temperature range of (700-750)°C [44].

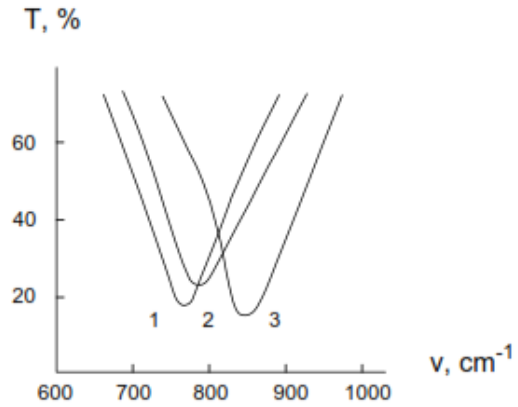

Figure 4: IR Absorption Spectra of Ge_3N_4 (1), germanium oxynitride film obtained by nitridation of germanium at temperature 700oC (2) and GeO2 (3).

Fig. 5(a) shows the dependence of the absorption coefficient (α) on the energy of photons (E=hν) for films obtained in different technological modes (temperature of nitridation of germanium: 600, 700 and 800°C).

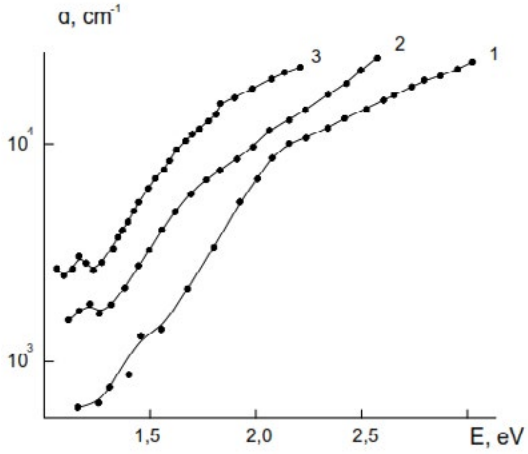

(a)

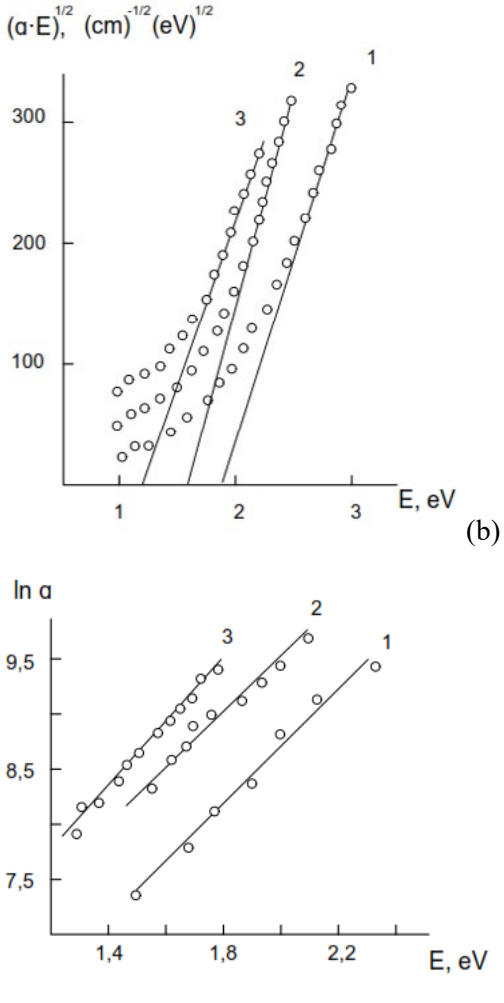

Figure 5: Electronic Absorption Spectra of Oxynitride Films Obtained by Nitridation of Germanium at Temperatures 600 (1), 700 (2) and 800oC (3) in coordinates: α – E (a), αE – E (b) and lnα – E (c).

It should be noted that, despite the similarity of these spectra with the spectra of amorphous elementary semiconductors (C, Si, Ge), they are characterized by somewhat elevated values of α below the fundamental absorption edge, which is determined by the degree of disorder of the amorphous network of the material.

The dependence of α on E is divided into three characteristic regions:

1) region of strong absorption ($\alpha>10^4$ cm^{-1}), which corresponds to interband transitions and is described by the equation $E=B(E - E_{opt})^2$, where B is a coefficient inversely proportional to the density of states near the conduction band and valence band, and Eopt is the optical width of the forbidden band [26-28]. The value of the coefficient B corresponds to the square of the slope (tan) of the dependence of the absorption coefficient on the photon energy in the coordinates $(\alpha E)^{1/2}$-E (Fig. 2b). For the considered temperatures of film production, these values are $9.7\cdot10^4$, $1.24\cdot10^5$ and $7.1\cdot10^4$ $eV\cdot cm^{-1}$, respectively. For comparison, we indicate that in amorphous hydrogenated silicon $B=4.5\cdot10^5$ $eV\cdot cm^{-1}$ [45]. The comparatively low values of B in our samples can be associated with a high density of states near the edges of the allowed bands. From this point of view, the most favorable temperature for film production is 700°C.

2) region of exponential dependence of α on E, called the Urbach's edge and which is described by the equation $\alpha=\alpha_0\exp(E/E_0)$, where α_0 is the pre-exponent, E_0 is the Urbach's energy [46,47]. E_0 can be determined by linearization of the given equation in lnα-E coordinates (Fig. 2 c, its value corresponds to the cotangent of the slope). The values of Urbach's energy for the considered modes of obtaining germanium oxynitride films are 0.38, 0.35, and 0.29 eV, respectively. The presence of the Urbach's "tail of states" is associated with defects caused by the violation of the long-range ordering of the structure in amorphous materials [48,49]. A decrease of E_0 with an increase of the film production temperature indicates relaxation of the structural network, which causes a decrease of the absorption caused by defects [50].

3) region characterized by the appearance of tails of the density of states caused by dangling bonds. This effect is associated with additional absorption at $\alpha<10^3$ cm^{-1} [50]. In this region, the dependence of α on E is weaker than exponential.

In conclusion, we note that the study of the electrophysical characteristics of these films determines the prospects for their

use in the creation of MIS (metal-insulator-semiconductor) devices and integrated circuits. The authors also plan to study the possibility of using germanium oxynitride films (along with crystalline Ge_3N_4) for photocatalytic applications [32,51-53].

4. Conclusion

A general equation is given that describes the scale growth-evaporation kinetic (sample mass change - time) curves during the interaction of gases with the surface of metals and compounds. Special cases of parabolic, cubic and fourth degree processes are discussed. Equations are also given for the case when scale formation is preceded by the process of gas etching of the metal surface. By evaporating the nitride formed on the germanium surface (along with the formation of volatile monoxide), a film of germanium oxyntride is deposited on a substrate located in the cold zone of the reactor. The optical characteristics of these films are studied. The dependence of the absorption coefficient on the energy of photons is divided into three characteristic regions: region of strong absorption ($\alpha>10^4$ cm^{-1}), which corresponds to interband transitions, region of exponential dependence of α on E (the Urbach's edge) and region characterized by the appearance of tails of the density of states caused by dangling bonds ($\alpha<10^3$ cm^{-1}).

References

1. Nakhutsrishvili. I., 2025. Oxidation kinetics of FeCr and FeCrAl alloys: Influence of secondary processes. *Johnson Mattey Techn. Rev., 1,* 38-44.
2. Smialek, J. L. (2023). Simplified paralinear oxidation analyses. *High Temperature Corrosion of Materials, 99*(5), 431-457.
3. Jones, E. S., Mosher, C. J., Speiser, R., & Spretnak, J. W. (1958). *The oxidation of molybdenum. Corrosion, 14*(1), 20-26.
4. Tedmon, C. S. (1966). The effect of oxide volatilization on the oxidation kinetics of Cr and Fe-Cr alloys. *Journal of the electrochemical society, 113*(8), 766.
5. Krejčí, J., Vrtílková, V., Gajdoš, P., & Rada, D. (2017). Proposal of new oxidation kinetics for sponge base E110 cladding tubes material. *EPJ Nuclear Sciences & Technologies, 3,* 18.
6. Yan, Y., Garrison, B. E., Howell, M., & Bell, G. L. (2018). High-temperature oxidation kinetics of sponge-based E110 cladding alloy. *Journal of Nuclear Materials, 499*, 595-612.
7. Pourbahari, B., & McDermid, J. R. (2023). Oxidation kinetics of Fe-(2-10) Mn-xSb alloys during annealing. *Materialia, 27*, 101698.
8. Aghaeian, S., Nourouzi, F., Sloof, W. G., Mol, J. M. C., & Böttger, A. J. (2023). Predicting the parabolic growth rate constant for high-temperature oxidation of steels using machine learning models. *Corrosion Science, 221,* 111309.
9. Feng, J., Tang, J., Chu, M., Zhao, Z., Liu, Z., Li, X., ... & Wang, X. (2023). Effect of Cr2O3 on the kinetics mechanism and microstructure of pellet during oxidation roasting process. *steel research international, 94*(5), 2200735.
10. Abd-El-Nabey, B. A., El-Housseiny, S., Abdel-Gaber, A. M., & Mohamed, M. E. (2023). Kinetics of oxidation of metals in the air at room temperature using EDX. *Results in Chemistry, 5,* 100876.
11. Estupinán-López, F., Orquiz-Muela, C., Gaona-Tiburcio, C., Cabral-Miramontes, J., Bautista-Margulis, R. G., Nieves-Mendoza, D., ... & Lopes, A. J. (2023). Oxidation Kinetics of Ti-6Al-4V Alloys by Conventional and Electron Beam Additive Manufacturing. *Materials, 16*(3), 1187.
12. Wajszel, D. (1963). A method for calculating paralinear constants for the formation of volatile scale. *Journal of the Electrochemical Society, 110*(6), 504.
13. Smeltzer, W. W., Haering, R. R., & Kirkaldy, J. S. (1961). Oxidation of metals by short circuit and lattice diffusion of oxygen. *Acta Metallurgica, 9*(9), 880-885.
14. Stringer, J. (1972). The functional form of rate curves for the high-temperature oxidation of dispersion-containing alloys forming Cr2O3 Scales. *Oxidation of Metals, 5*(1), 49-58.
15. Atkinson, H. V. (1985). A review of the role of short-circuit diffusion in the oxidation of nickel, chromium, and nickel-chromium alloys. *Oxidation of Metals, 24,* 177-197.
16. Liu, T. K., & Bautista, R. G. (1981). Prediction of the global volatilization rate of gas-metal-alloy reaction systems—Method of calculation. *Oxidation of Metals, 16,* 243-252.
17. Carrette, F., Guinard, L., & Pieraggi, B. (2002). Kinetics of corrosion products release from nickel-base alloys corroding in primary water conditions. *A new modeling of release, Water Chemistry in Nuclear Reactor System*, 22-26.
18. Ihara, Y., Ohgame, H., Sakiyama, K., & Hashimoto, K. (1983). The corrosion behaviour of chromium in hydrogen chloride gas and gas mixtures of hydrogen chloride and oxygen at high temperatures. *Corrosion Science, 23*(2), 167-181.
19. Smialek, J. L., & Jacobson, N. S. (2014). Oxidation of high-temperature aerospace materials. *High temperature materials and mechanisms*, 95-162.
20. Nakhutsrishvili, I. (2020). Study of Growth and Sublimation of Germanium Nitride Using the Concept of Tedmon's Kinetic Model. *Oriental Journal of Chemistry, 36*(5), 850.
21. Davis, H. H., Graham, H. C., & Kvernes, I. A. (1971). Oxidation behavior of Ni-Cr-1ThO2 alloys at 1000 and 1200° C. *Oxidation of Metals, 3*(5), 431-451.
22. Nelson, A. T., Sooby, E. S., Kim, Y. J., Cheng, B., & Maloy, S. A. (2014). High temperature oxidation of molybdenum in water vapor environments. *Journal of nuclear materials, 448*(1-3), 441-447.
23. Pujilaksono, B., Jonsson, T., Halvarsson, M., Panas, I., Svensson, J. E., & Johansson, L. G. (2008). Paralinear oxidation of chromium in O 2+ H 2 O environment at 600–700 C. *Oxidation of Metals, 70,* 163-188.
24. Guangwei, W., Yanxiang, L., Jianliang, Z., Kuo-Chih, C., & Xinmei, H. (2014). Reaction of CVD BN ceramics in water vapor at 1023–1173 K using different kinetic model. *Journal of the Ceramic Society of Japan, 122*(1430), 889-894.
25. Kruk, A., Gil, A., Lech, S., Cempura, G., Agüero, A., & Czyrska-Filemonowicz, A. (2021). Multiscale Characterization of an Oxide Scale Formed on the Creep-Resistant ATI 718Plus Superalloy during High-Temperature Oxidation. *Materials, 14*(21), 6327.
26. Dryepondt, S., Pint, B. A., & Maziasz, P. J. (2015). New creep-resistant cast alloys with improved oxidation resistance

in water vapor at 650–800 C. *Frontiers in Materials, 2*, 55.
27. Peng, J., Pillai, R., Romedenne, M., Pint, B. A., Muralidharan, G., Allen Haynes, J., & Shin, D. (2021). Data analytics approach to predict high-temperature cyclic oxidation kinetics of NiCr-based Alloys. *npj Materials Degradation, 5*(1), 41.
28. Nakhutsrishvili, I. (2016). Some Formal Aspects of Tedmon's Kinetics: Growth and Sublimation of Ge3N4. *Journal of Technical Science and Technologies, 5*(1), 19-25.
29. Aronishidze, M., Nakhutsrishvili, I., Vardosanidze, Z., et al., (2015). Some aspects of gas etching of monocrystalline germanium surface. *Prooc Georgian Acad Sci, 41,* 361-364.
30. Sepashvili, N., Adamia, Z., Kokhreidze, R. Nakhutsrishvili, I. (2024). Formation-evaporation of germanium monoxide in water vapor and (Ge+GeO2) films. Engineering and Applied Sci., 1, in press.
31. Mallem, K., Jagadeesh Chandra, S. V., Ju, M., Dutta, S., Ramana, C. H., Hussain, S. Q., ... & Yi, J. (2020). Influence of Ultra-Thin Ge3N4 Passivation Layer on Structural, Interfacial, and Electrical Properties of HfO_2/Ge Metal-Oxide–Semiconductor Devices. *Journal of Nanoscience and Nanotechnology, 20*(2), 1039-1045.
32. Ma, Y., Wang, M., & Zhou, X. (2020). First-principles investigation of β-Ge3N4 loaded with RuO2 cocatalyst for photocatalytic overall water splitting. *Journal of Energy Chemistry, 44,* 24-32.
33. Huang, Z., Su, R., Yuan, H., Zhang, J., Chen, F., Shen, Q., & Zhang, L. (2018). Synthesis and photoluminescence of ultra-pure α-Ge3N4 nanowires. *Ceramics International, 44*(9), 10858-10862.
34. Kim, C., Hwang, G., Jung, J. W., Cho, S. H., Cheong, J. Y., Shin, S., ... & Kim, I. D. (2017). Fast, scalable synthesis of micronized Ge3N4@ C with a high tap density for excellent lithium storage. *Advanced Functional Materials, 27*(14), 1605975.
35. Maggioni, G., Carturan, S. A. R. A., Fiorese, L., Pinto, N., Caproli, F., Napoli, D. R., ... & Mariotto, G. (2017). Germanium nitride and oxynitride films for surface passivation of Ge radiation detectors. *Applied surface science, 393*, 119-126.
36. Yayak, Y. O., Sozen, Y., Tan, F., Gungen, D., Gao, Q., Kang, J., ... & Sahin, H. (2022). First-principles investigation of structural, Raman and electronic characteristics of single layer Ge3N4. *Applied Surface Science, 572*, 151361.
37. Rzhanov, A. V., & Neizvestny, I. G. (1979). Germanium MIS structures. *Thin Solid Films, 58*(1), 37-42.
38. Hsu, B. C., Lin, C. H., Kuo, P. S., Chang, S. T., Chen, P. S., Liu, C. W., ... & Kuan, C. H. (2004). Novel MIS Ge-Si quantum-dot infrared photodetectors. *IEEE electron device letters, 25*(8), 544-546.
39. Fukuda, Y., Kato, K., Toyota, H., Ono, T., Nagasato, Y., & Ueno, T. (2006). Electrical properties of germanium oxynitride and its interface with germanium prepared by electron-cyclotron-resonance plasma oxidation and nitridation. *Japanese journal of applied physics, 45*(9S), 7351.
40. Kutsuki, K., Okamoto, G., Hosoi, T., Shimura, T., & Watanabe, H. (2009). Germanium oxynitride gate dielectrics formed by plasma nitridation of ultrathin thermal oxides on Ge (100). *Applied Physics Letters, 95*(2).
41. Wang, J., Asakura, Y., & Yin, S. (2020). Synthesis of zinc germanium oxynitride nanotube as a visible-light driven photocatalyst for NOx decomposition through ordered morphological transformation from Zn2GeO4 nanorod obtained by hydrothermal reaction. *Journal of hazardous materials, 396,* 122709.
42. Du, S. J., Li, X. X., Tian, Y., Liu, Y. Y., Jia, K., Tang, Z. Z., ... & Lv, S. S. (2024). Analyzing the surface passivity effect of germanium oxynitride: a comprehensive approach through first principles simulation and interface state density. *Nuclear Science and Techniques, 35*(5), 45.
43. Wardosanidze, Z. V., Nakhutsrishvili, I., & Kokhreidze, R. Conditions of Formation of α-and β-Modifications of Ge3N4 and Preparation of Germanium Oxynitride Dielectric Films. *Journal of Coating Science and Technology, 11*.
44. Bayraktaroglu, B., Johnson, R. L., Langer, D. W., & Mier, M. G. (1980). GERMANIUM (OXY) NITRIDE BASED SURFACE PASSIVATION TECHNIQUE AS APPLIED TO GaAs & InP. In *The Physics of MOS Insulators* (pp. 207-211). Pergamon.
45. Toudert, J., & Serna, R. (2017). Interband transitions in semi-metals, semiconductors, and topological insulators: a new driving force for plasmonics and nanophotonics. *Optical Materials Express, 7*(7), 2299-2325.
46. Ekimov, A. I., & Safarov, V. I. (2023). Optical Orientation of Carriers in Interband Transitions in Semiconductors. *JETP Letters, 118*(Suppl 1), S38-S40.
47. Bala, K. J., Peter, A. J., & Lee, C. W. (2019). Interband and intersubband optical transition energies in a Ga0. 7In0. 3N/GaN quantum dot. *Optik, 183,* 1106-1113.
48. Sakata, Y., Hayashi,J., Yamaraka,M., Karasawa,H. (1981). A new characterization parameter for hydrogenated amorphous silicon. *Applied Physics, 52*, 4334-4336.
49. Ugur, E., Ledinský, M., Allen, T. G., Holovský, J., Vlk, A., & De Wolf, S. (2022). Life on the Urbach edge. *The journal of physical chemistry letters, 13*(33), 7702-7711.
50. Holovský, J., Ridzoňová, K., Peter Amalathas, A., Conrad, B., Sharma, R. K., Chin, X. Y., ... & De Wolf, S. (2023). Below the Urbach Edge: Solar Cell Loss Analysis Based on Full External Quantum Efficiency Spectra. *ACS Energy Letters, 8*(7), 3221-3227.
51. Sato, J., Saito, N., Yamada, Y., Maeda, K., Takata, T., Kondo, J. N., ... & Inoue, Y. (2005). RuO2-loaded β-Ge3N4 as a non-oxide photocatalyst for overall water splitting. *Journal of the American Chemical Society, 127*(12), 4150-4151.
52. Lee, Y., Watanabe, T., Takata, T., Hara, M., Yoshimura, M., & Domen, K. (2006). Effect of high-pressure ammonia treatment on the activity of Ge3N4 photocatalyst for overall water splitting. *The Journal of Physical Chemistry B, 110*(35), 17563-17569.
53. Maeda, K., & Domen, K. (2007). New non-oxide photocatalysts designed for overall water splitting under visible light. *The journal of physical chemistry C, 111*(22), 7851-7861.